6290 *Macromolecules* **2009**, *42*, 6290–6299
DOI: 10.1021/ma900453c

Macromolecules
ARTICLE

High Precision Transport Properties of Cylinders by the Boundary Element Method

Sergio R. Aragon* and Dina Flamik

Department of Chemistry & Biochemistry, San Francisco State University, San Francisco, California 94132

Received February 28, 2009; Revised Manuscript Received June 24, 2009

ABSTRACT: In this work we apply the boundary element method to obtain very precise computations of the hydrodynamic transport properties for rectangular, sphero, and open cylinders. This work numerically solves the exact integral equations for Stokes flow with stick boundary conditions and includes the tensor values for the translational and rotational diffusion coefficients, and the intrinsic viscosity for three types of cylinders with axial ratios between 1 and 100. We describe the properties of the triangular tessellations that yield essentially numerically exact properties, with estimated uncertainties of 0.07% or better. The data are summarized by fairly simple mathematical expressions as a function of the axial ratio of the cylinders which are constructed to satisfy the correct asymptotic expressions, yielding formulas that are valid for $1 \leq p < \infty$. The end effects for the three different types of caps are discussed—such end effects are noticeable for small axial ratios and become unimportant for large axial ratios. The open cylinders behave in a similar fashion to the closed end cylinders, despite the absence of caps. For the intrinsic viscosity, we introduce a new formula with correct asymptotic limits and high accuracy at unit axial ratio which greatly improves the description over traditional expressions derived from slender body theory. We compare our results with previous formulas available in the literature for different types of cylinders and conclude that, except for the path integral method results, most previous work has significant inaccuracies. The expressions obtained in this work, will be useful in the description of the transport properties of interesting macromolecular structures such as carbon nanotubes, microtubules, and viruses.

I. Introduction

Cylindrical shapes appear in nature in a variety of molecular forms from single wall carbon nanotubes[1] (SWCNT), some viruses such as TMV[2] and M13,[3] DNA oligomers,[4] and cellular microtubules.[5] In many instances, it is of interest to characterize these species in solution, and hydrodynamic measurements such as sedimentation, translational diffusion, rotational diffusion, or intrinsic viscosity can be carried out. In this paper, we present very precise computations of such properties for three types of cylinders: rectangular cylinders, open (uncapped) cylinders, and spherocylinders, using the boundary element method. These shapes can all be assumed by SWCNT, for example. In previous work,[6] we have reported on the development of a very precise boundary element method (BE) and a program suite (BEST) for the computation of transport tensors of arbitrarily shaped bodies under the stick boundary condition. BEST was thereafter applied to the computation of transport properties[7,8] of proteins, including translational diffusion, the rotational diffusion tensor, and the intrinsic viscosity, and to study the flow stagnation in protein pockets.[9] In addition, we have used the BE method to investigate the short comings of the preaveraged hydrodynamic interaction,[10] an attractive approximation that simplifies the Oseen tensor by its orientational average.

The boundary element method allows the computation of transport properties with unprecedented accuracy because it depends on an exact formulation of the Stokes flow equations[11−13] and does not depend at all on approximate hydrodynamic interaction tensors commonly used in bead representations of molecules.[14] In addition to this laboratory, several other authors have used the boundary element method to compute diffusion coefficients with stick[15] or slip boundary conditions,[16,17] intrinsic viscosity,[18] and electrophoretic mobilities[19−21] with great success. Thus, the boundary element method is well established and is a method of choice for accurate and precise computations.

Despite the presence of cylindrical symmetry, the transport properties of cylinders are not obtainable analytically in closed form—the closest shape for which exact analytical solutions exist is the prolate spheroid.[22−24] General properties of the fluid flow past cylinders can be addressed in the small Reynolds number region by dimensional arguments such as those presented in Batchelor.[25] However, the first detailed calculations of the transport properties of cylinders are those of Broersma,[26,27] where he obtained approximate analytical expressions for the rotational diffusion constant for end-over-end tumbling and the average viscous drag for translational motion of rectangular cylinders. Twenty years later, Broersma[28] updated his calculations with improved results. Yamakawa[29] studied the viscoelastic properties of rectangular cylinders with approximate analytical methods. In the mid-1980s, the first completely numerical calculations for the translational and rotational motion of rectangular cylinders using "bead hydrodynamics" by Tirado and Garcia de la Torre[30,31] (TG) appeared, as well as the approximate boundary element method treatment by Yoshisaki and Yamakawa[32] (YY) which additionally included the intrinsic viscosity. YY made a detailed study of the end-effects by capping their cylinders with an ellipsoidal cross-section which includes the spherocylinder studied in this work. Their treatment did not extend to the rectangular cylinder case, which is a limiting shape of their blunt cylinder. In more recent work, Ortega and Garcia de la Torre[33] have also computed the intrinsic viscosity of rectangular cylinders with a numerical bead method. We make detailed comparisons of these

*Corresponding author. E-mail: aragons@sfsu.edu.

 Published on Web 08/04/2009

works with our high precision computations below and generally find that the older expressions have significant inaccuracies and have limited range of validity in the axial ratio.

The diffusion properties of nonspherical objects are described by tensors. For the case of cylindrical bodies, there are two distinct eigenvalues of the diffusion tensors. Due to the limited ability of experiments to distinguish the components of the translational diffusion tensor, previous workers such as TG, OG, and YY have computed only the average of this tensor. We compute the separate eigenvalues as well as the average in this work. In the case of rotation, the different eigenvalues are weighted very differently in different experiments and thus separate calculations of these quantities are needed and most workers have done so. We will demonstrate below that the BE method provides unparalleled accuracy and precision in the computation of transport properties, far surpassing that obtainable by bead hydrodynamics and other methods.

There is one approximate method that offers some advantages and yields high precision in what it computes: the path integral method of Douglas and co-workers.[34,35] This method exploits an electrostatic analogy but is generally not equivalent to a computation which preaverages the Oseen tensor. Since the computation uses a stochastic method, the advantage is that the computational efficiency grows linearly with the number of trajectories that must be launched to compute the capacity and polarizability of the body. The boundary element method, on the other hand is much more computationally demanding, as discussed in detail below. The relationship of the electrical properties to the hydrodynamic ones is, in general, only approximate. Our previously published work[10] on the computation of the precise transport properties from the preaveraged hydrodynamic interaction, by the same boundary element methods used in the present work, shows that the average translational friction can be computed for arbitrarily shaped bodies to an accuracy better than 1%. For the translational diffusion the electrostatic capacity of a metallic body is effectively equivalent to a preaveraged hydrodynamic interaction, thus, we expect that the path integral method will compare very favorably with our methods for the translational diffusion and serve as an independent check that discrepancies larger than 1% actually do represent numerical inaccuracies in other works that we compare to below. In addition, recent work by Mansfield and Douglas[36] has shown that the typical 5% inaccuracy in the metallic body polarizability approximant for the intrinsic viscosity can be effectively eliminated by an intricate procedure that works very well for the case of cylinders, and possibly for other shapes. We will compare our work in detail with this method, noting that, by nature, no tensor transport properties can be computed from it. In the next section, we briefly review the basic equations of the BE method.

II. Theory: The Boundary Element Method for Stick Boundary Conditions

Taking the solvent as a continuum is an excellent approximation for the diffusion of small bodies in a liquid and the governing equations for the computation of the hydrodynamic transport properties are the Navier−Stokes equations of fluid flow. In the limit of small Reynolds number, as appropriate for the diffusion process, the equations are known as the Stokes or creeping flow equations.[11] Whereas bead methods aim to solve a mobility problem, which cannot be formulated exactly, an alternative method is to solve a resistance problem, which can be formulated exactly. As is shown below, once one has precise friction tensors, it is straightforward to compute the diffusion tensors. In the mid 1970s, Youngren and Acrivos[12] presented an effective method for the numerical solution to the *exact surface integral* representation of the velocity field for the creeping flow equations.

For the case of macromolecules in aqueous solvents, "stick" boundary conditions are appropriate. In this case, the velocity field of the flow, $\mathbf{v}(\mathbf{y})$ at position $\mathbf{y}$ in the fluid, can be written as an integral over the particle surface (sp),

$$\mathbf{v}(\mathbf{y}) = \mathbf{u}_o(\mathbf{y}) + \int_{sp} \overleftrightarrow{\mathbf{T}}(\mathbf{x},\mathbf{y}) \cdot \mathbf{f}(\mathbf{x})\, dS_x \tag{1}$$

where $\mathbf{u}_0(\mathbf{y})$ is the flow velocity of the fluid if the particle was not there (which can be taken to be zero for diffusive motion), and $\overleftrightarrow{\mathbf{T}}(\mathbf{x},\mathbf{y})$ is the Oseen hydrodynamic interaction tensor. The surface stress force, $\mathbf{f}(\mathbf{x})$ is the unknown quantity that we must obtain. Once this quantity is known, not only can the transport properties of the macromolecule can be directly computed, but also the velocity field for any point $\mathbf{y}$ outside the body. The computation of the velocity field outside the body is then a two step process. First, we take the point $\mathbf{y}$ on the surface and move the body with a known velocity field to obtain the unknown surface stress forces on the surface of the body; second, we can then use eq 1 to compute the velocity field at any other point $\mathbf{y}$ in the fluid, for that body motion. The Oseen tensor is given by[11,37]

$$\overleftrightarrow{\mathbf{T}}(\mathbf{x},\mathbf{y}) = \frac{1}{8\pi\eta|\mathbf{x}-\mathbf{y}|}\left[\overleftrightarrow{\mathbf{I}} + \frac{(\mathbf{x}-\mathbf{y})(\mathbf{x}-\mathbf{y})}{|\mathbf{x}-\mathbf{y}|^2}\right] \tag{2}$$

Since eq 1 is an integral equation, the solution requires an approximate numerical method. The method, however, can be iterated to obtain arbitrary precision. The first step is to discretize the surface by replacing it with a collection of N patches that smoothly tile the molecular surface and to consider the velocity field for points $\mathbf{y}$ on the surface of the arbitrarily shaped body. We can then write,

$$sp = \sum_{j=1}^{N} \Delta_j \tag{3}$$

We place the coordinate $\mathbf{X}_j$ at the center of the small patch Δ_j and take the surface stress force $\mathbf{f}(\mathbf{x})$ to be a constant over the entire patch area. This is the basic approximation: it is clear that it will become a better and better approximation as the patch is made small. Thus, an extrapolation to zero size patch leads to a very precise value for the transport properties and the unknown surface stress forces. With this approximation, eq 1 becomes a set of $3N$ equations for the $3N$ unknowns, $\mathbf{f}_j = \mathbf{f}(\mathbf{x}_j)$,

$$\mathbf{v}(\mathbf{y}_k) = \sum_{j=1}^{N} \overleftrightarrow{\mathbf{G}}_{kj} \cdot \mathbf{f}_j \tag{4}$$

The centerpiece of this set of equations is a set of N completely known 3×3 matrices of coefficients that contain all geometric information, the integrals of the Oseen tensor over a surface patch,

$$\overleftrightarrow{\mathbf{G}}_{kj} = \int_{\Delta_j} \overleftrightarrow{\mathbf{T}}(\mathbf{x},\mathbf{y}_k)\, dS_x \tag{5}$$

In addition to the introduction of a robust regularization method, the other significant advance made in our work[6] is the essentially exact integration of the Oseen tensor in the above expression. The set of $3N$ equations can be written all at once

$$\begin{bmatrix} \mathbf{v}_1 \\ .. \\ .. \\ \mathbf{v}_N \end{bmatrix}_{3N\times 1} = \begin{bmatrix} \overleftrightarrow{\mathbf{G}}_{11} & .. & .. & \overleftrightarrow{\mathbf{G}}_{1N} \\ .. & .. & .. & .. \\ .. & .. & .. & .. \\ \overleftrightarrow{\mathbf{G}}_{N1} & .. & .. & \overleftrightarrow{\mathbf{G}}_{NN} \end{bmatrix}_{3N\times 3N} \begin{bmatrix} \mathbf{f}_1 \\ .. \\ .. \\ \mathbf{f}_N \end{bmatrix}_{3N\times 1} \tag{6}$$

from which the unknown surface stress forces can be readily obtained by matrix inversion of the $3N \times 3N$ super matrix $\vec{\vec{\mathbf{G}}}$, as shown schematically in eq 7:

$$[\mathbf{f}]_{3N\times 1} = [\vec{\vec{\mathbf{G}}}]_{3N\times 3N}^{-1}[\mathbf{v}]_{3N\times 1} \tag{7}$$

The total force and torque on the body can be computed from the surface stress forces and these are directly related to the friction tensors ($\vec{\vec{\mathbf{K}}}$) of the body,

$$\mathbf{F} = \sum_{j=1}^{N} \mathbf{f}_j(\mathbf{x})\Delta_j = -\vec{\vec{\mathbf{K}}}_{tt}\cdot\mathbf{v}_\mathrm{P} - \vec{\vec{\mathbf{K}}}_{tr}\cdot\boldsymbol{\omega}_\mathrm{p} \tag{8}$$

$$\mathbf{T} = \sum_{j=1}^{N} \mathbf{x}_p \times \mathbf{f}_j(\mathbf{x})\Delta_j = -\vec{\vec{\mathbf{K}}}_{rt}\cdot\mathbf{v}_\mathrm{p} - \vec{\vec{\mathbf{K}}}_{rr}\cdot\boldsymbol{\omega}_\mathrm{p} \tag{9}$$

The particle can be assumed to have specific translation velocity $\mathbf{v}_\mathrm{p}$ and angular velocity $\boldsymbol{\omega}_\mathrm{p}$ (for example $\boldsymbol{\omega}_\mathrm{p} = 0$ and $\mathbf{v}_\mathrm{p} = (\mathbf{v}_x,0,0)$) to solve the above equations. Thus, six calculations suffice to determine all components of the friction tensors. The friction tensors form part of a larger 6×6 tensor that contains information about the pure translational friction (tt), the pure rotational friction (rr), and the coupling that may exist between these (rt and tr). There are actually only three independent friction tensors because the $\vec{\vec{\mathbf{K}}}$ tensor is the transpose of the $\vec{\vec{\mathbf{K}}}$ tensor. This coupling is insignificant unless the body has a screw-like axis of symmetry.[38] The diffusion tensors are finally obtained from the friction tensors by an easy 3×3 matrix inversion,

$$\vec{\vec{\mathbf{D}}}_t = kT[\vec{\vec{\mathbf{K}}}_{tt} - \vec{\vec{\mathbf{K}}}_{tr}\cdot\vec{\vec{\mathbf{K}}}_{rr}^{-1}\cdot\vec{\vec{\mathbf{K}}}_{rt}]^{-1} \tag{10}$$

$$\vec{\vec{\mathbf{D}}}_r = kT[\vec{\vec{\mathbf{K}}}_{rr} - \vec{\vec{\mathbf{K}}}_{tr}\cdot\vec{\vec{\mathbf{K}}}_{tt}^{-1}\cdot\vec{\vec{\mathbf{K}}}_{rt}]^{-1} \tag{11}$$

These formulas need one last correction. It so happens that the value of the rotational diffusion tensor in eq 11 is independent of the choice of origin for the location of the surface patches of the body, however, the same is not true for the translational diffusion tensor in eq 10. There is one preferred center, called the "center of diffusion", which must be selected in order to get the correct measurable value for translation. The procedure to achieve this entails an analysis of the transformation properties of the tensors with respect to translations which has been given by Brenner.[38] We will omit most of the tensor equations for brevity. Suffice it to say that in the center of diffusion, the $\vec{\vec{\mathbf{D}}}_{tr}$ tensor, which is given by

$$\vec{\vec{\mathbf{D}}}_{tr} = -\vec{\vec{\mathbf{K}}}_{tt}^{-1}\cdot\vec{\vec{\mathbf{K}}}_{tr}\cdot\vec{\vec{\mathbf{D}}}_r \tag{12}$$

must be symmetric. If the origin that we used is not at the center of diffusion, the tensor in eq 12 will be asymmetric. The asymmetry present in the rotation-translation coupling tensor of eq 12, can be used to calculate the translation vector to the center of diffusion to correct the value of $\vec{\vec{\mathbf{D}}}$. This procedure has been implemented in our Fortran program BEST. However, in the case of cylindrical particles, the center of diffusion coincides with the centroid of the body, and there is no translation-rotation coupling, so $\vec{\vec{\mathbf{K}}}_{\mathrm{tr}} = 0$. The expressions in eqs 10 and 11 thus reduce to simpler forms in which the subtracted part in the inverse is absent. BEST handles this automatically—no special symmetry considerations are required in the input.

To compute different transport properties, one selects appropriate flows that specify the particular form of $\mathbf{v}(\mathbf{y})$. For the intrinsic viscosity, one selects five elementary shear flows[39]

$$\mathbf{v}_0^{(1)}(\mathbf{y}) = \frac{1}{2}\mathbf{E}^{(1)}\cdot(\mathbf{y}-\mathbf{d}) \tag{13}$$

where $\mathbf{d}$ is the center of viscosity (the point where the dissipation of energy is minimized) and

$$\mathbf{E}^{(1)} = \gamma(\mathbf{e}_1\mathbf{e}_2+\mathbf{e}_2\mathbf{e}_1) \tag{14a}$$

$$\mathbf{E}^{(2)} = \gamma(\mathbf{e}_1\mathbf{e}_3+\mathbf{e}_3\mathbf{e}_1) \tag{14b}$$

$$\mathbf{E}^{(3)} = \gamma(\mathbf{e}_1\mathbf{e}_3+\mathbf{e}_3\mathbf{e}_1) \tag{14c}$$

$$\mathbf{E}^{(4)} = \gamma(\mathbf{e}_1\mathbf{e}_1-\mathbf{e}_2\mathbf{e}_2) \tag{14d}$$

$$\mathbf{E}^{(5)} = \gamma(\mathbf{e}_1\mathbf{e}_1-\mathbf{e}_3\mathbf{e}_3) \tag{14e}$$

with γ being the shear gradient and $\mathbf{e}_\alpha$ being a unit vector along axis α in the laboratory frame of reference. For a particle of volume V_p and molecular weight M, $[\eta] = \chi N_\mathrm{A} V_\mathrm{p}/M$, where N_A is Avogadro's number and χ, the viscosity factor, is a function of particle shape and surface roughness. When the viscosity factor is formulated in terms of the boundary element method, one obtains,

$$\chi = -\frac{1}{\eta_\mathrm{o}\gamma V_\mathrm{p}}\int_{\mathrm{sp}} (\mathbf{y}-\mathbf{d})_\mathrm{b}\cdot\mathbf{f}_\mathrm{a}\,\mathrm{d}S_x \tag{15}$$

where subscripts a and b denote vector components along the flow direction and the direction of greatest shear, respectively. Discretizing the surface integral and then averaging over all orientations of the particle, Allison[39] has shown that

$$\chi = \frac{1}{5}(\xi_{12}^{(1)} + \xi_{13}^{(2)} + \xi_{23}^{(3)}) + \frac{1}{15}(\xi_{11}^{(4)} + \xi_{33}^{(4)} - 2\xi_{22}^{(4)} + \xi_{11}^{(5)} + \xi_{22}^{(5)} - 2\xi_{33}^{(5)}) \tag{16a}$$

where

$$\xi_{\alpha\beta}^{(l)} = -\frac{1}{2\eta_\mathrm{o}\gamma V_\mathrm{p}}[\sum_{j=1}^{N}(\mathbf{y}_j-\mathbf{d})\cdot(\mathbf{e}_\alpha\mathbf{e}_\beta + \mathbf{e}_\beta\mathbf{e}_\alpha)\cdot\Delta_j\mathbf{f}_j^{(l)}] \tag{16b}$$

with subscript j representing the surface elements and superscript l representing the five elementary shear fields for which the viscosity factor is evaluated. The area of boundary element j is denoted Δ_j, the stress force of shear field l on surface element j is denoted $\mathbf{f}_j^{(l)}$, and the *incenter* (the center of the largest circle inscribable inside the triangle) of boundary element j in the particle frame of reference is denoted $\mathbf{y}_j$. These equations are programmed in the viscosity subroutine of BEST. In the cylinder case, the center of viscosity also coincides with the centroid of the cylinder, thus simplifying the computation.

III. Triangulations of Cylindrical Bodies and Extrapolations to Infinite Triangles

The basic input to BEST is a triangulation for the surface of the body of interest. The accuracy of the computation depends on proper triangulations, so we describe these in detail in this section. The triangulations have been obtained to high precision in Mathematica.[40] In order to eliminate the discretization inaccuracy, one has to compute the transport properties for a sequence of finer and finer triangulations and then extrapolate the properties to infinite number of triangles. Thus it is crucial to define the special features of the shape of interest with increasing accuracy as the refinement proceeds. Our cylindrical shapes are

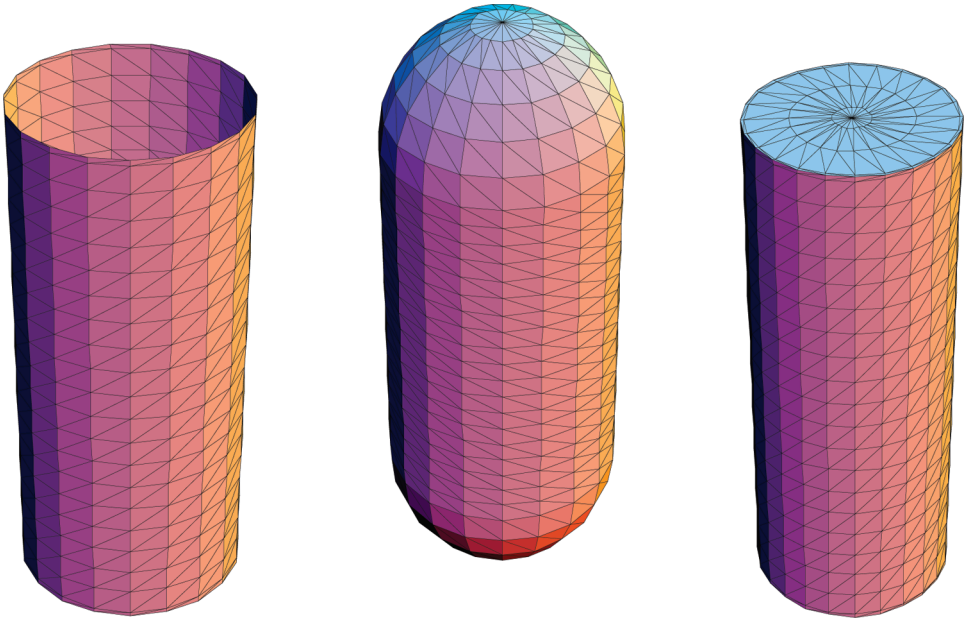

Figure 1. Triangular tessellations for open, sphero, and rectangular cylinders. The number of triangles shown here (about 1000) corresponds to the smallest number of triangles used. Note the presence of the thin rings near the sharp edge in the open and rectangular cylinders.

constructed from sections that handle specific features. Typical triangulations are shown in Figure 1 for the three shapes we treat in this work. The coordinates of the triangles are computed to 12 digits to avoid round-off inaccuracy in the computation. A set of 4−5 refinements of the triangulations are generated for each axial ratio, with increasing number of triangles. The refinements are constructed such that the number of triangles increases along the periphery, along the length, and the number of latitude rings in the caps increases. In addition, and most importantly, there is a thin ring near the sharp edge that places points and small triangles near this singularity in the shape. As the refinement proceeds, the ring gets thinner, approaching the edge from both the cap and along the length of the cylinder. In this fashion, the sharpness of the edge is defined better and better as the refinement proceeds. With this type of triangulation strategy, the extrapolations of the properties, described in detail in the following, completely define the smoothness of the circumference, the flatness or roundedness of the cap, and the sharpness of the edge in the open and rectangular cylinders.

As noted above, the only approximation that we make in the solution of the integral equation is to assume that the surface stress is constant over a small triangle. This procedure is exact in the limit of infinitely small triangle, thus we can solve the equation effectively exactly by extrapolating the results to infinite number of triangles. The scheme we use for this extrapolation is to set the value of any computed hydrodynamic property, say, $P = P(N)$, and expand this function of the number of triangles, N, in a Laurent series

$$P(N) = P_o + a/N + b/N^2 + \ldots \quad (17)$$

This extrapolation will be precise when the range of N used is such that the graph is effectively linear, with very little curvature. A typical example least-squares fit is shown in Figure 2. We have used quadratic fits even though the lines have no visible curvature because the data are very precise. An important statistic of the fit is the "TStat" provided by Mathematica. A magnitude larger than 1 indicates that the basis function used in the fit is statistically supported by the data. This observation is key in devising accurate formulas to represent the data as a function of axial ratio and will be mentioned again below. The data fit in

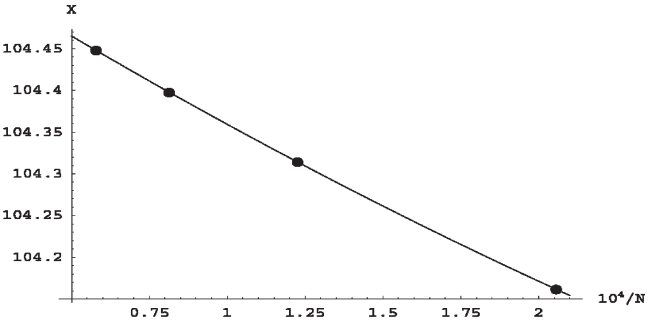

Figure 2. Least-squares fit line for the viscosity factor of a rectangular cylinder of axial ratio = 40. The actual data and statistical results are given in the text.

Figure 2 corresponds to the viscosity factor for a rectangular cylinder of axial ratio 40:

$$\left\{\left\{\frac{1}{17272}, 104.448\right\}, \left\{\frac{1}{12296}, 104.397\right\}, \left\{\frac{1}{8160}, 104.314\right\}, \left\{\frac{1}{4864}, 104.161\right\}\right\}$$

The first member of the pair is $1/N$, and the second is the value of the dimensionless viscosity factor. Note that BEST gives output to 6 significant figures, and the slope of this data is small − the variation over a factor of more than 3 in the number of triangles appears in the fourth and fifth significant digits. Figure 2 shows that the graph is in the linear region, yet the small amount of curvature is well-defined statistically, demonstrating the high precision of this data set. The actual fit data and statistical output of Mathematica is shown in Table 1.

We note that the standard error (SE) in the intercept, the viscosity factor at infinite number of triangles, is 0.001, validating the sixth digit in the extrapolation, and the number of digits provided by BEST. Thus the value of the intercept is 104.579 in this example.

For each of the cylinder shapes we have studied, the five different values of the transport properties were computed in the

Table 1. Analysis of Viscosity Raw Data[a]

parameter	value	standard error	T_{stat}
1	104.579	0.00111243	94009.5
x	−2353.82	19.5104	−120.64
x^2	1.57524×10^6	71695.9	21.97

[a] $R^2 = 1.0$ and estimated variance $= 1.01 \times 10^{-7}$.

fashion described above for a list of axial ratios between 1 and 100. The five transport properties are the two different eigenvalues of each of the translational diffusion and rotational diffusion tensors, and the viscosity factor. The extrapolated values at each axial ratio are the raw data that is represented by a mathematical model to high precision. In the next section, we present the formulas that represent this raw data and discuss the accuracy and precision of the results.

IV. Formulas for the Transport Properties of Cylinders

The objective in this section is to provide a set of formulas to compute the transport properties as a function of the length of a cylinder, L, and its axial ratio, $p = L/d$, where d is the diameter. Since our formulas are very precise, suitable ratios of particular properties are easily calculated for ease of extracting these parameters from experimental data. We do not present such ratios here, preferring to focus on the fidelity of the formulas to represent the precision inherent in the raw data set. We first present the basic results and then discuss how the functional forms were selected. We note that the choice of correct asymptotic forms for the cylinder transport properties allows us to obtain formulas that are valid for the complete range of axial ratios: $1 \leq p \leq \infty$. Thus, our results for finite axial ratios $p < 100$ are suitably extrapolated to large axial ratios.

The basic transport properties will be written down as follows. The two eigenvalues of the diffusion coefficients are called the perpendicular ($\perp$) and the parallel ($\parallel$) component, respectively. The basic forms for the diffusion tensor components are given in terms of a robust asymptotic function, typically $\ln(p)$, and a shape function $X(p)$, which has been determined by least-squares fitting. The shape function is different for every property and is given below for each of the shapes following the basic expressions.

IV.1. Translational Diffusion. Following the asymptotic forms for the case of ellipsoids,[11] the two components of the translational diffusion tensor are given by

$$D_\tau^\perp = \frac{kT}{4\pi\eta L}[\ln(p) + X_\tau^\perp(p)] \tag{18}$$

$$D_\tau^\parallel = \frac{kT}{4\pi\eta L}[2\ln(p) + X_\tau^\parallel(p)] \tag{19}$$

The average value of the translational diffusion tensor is given by

$$D_\tau = \frac{(2D_\tau^\perp + D_\tau^\parallel)}{3} = \frac{kT}{3\pi\eta L}[\ln(p) + X_\tau(p)] \tag{20}$$

where

$$X_\tau = \frac{1}{4}(2X_\tau^\perp + X_\tau^\parallel)$$

The axial ratio dependence of the eigenvalues of the translational diffusion tensor is shown in Figures 3 and 4. The functional forms of the shape function for each of the three shapes are given in Table 2. The precision to which the expressions reproduce the raw data is given in the column labeled "prec.", a number that is comparable to the precision of the raw data itself and is at most 0.07%. Thus the raw data are not included in the plots since the fits look perfect to any printable resolution.

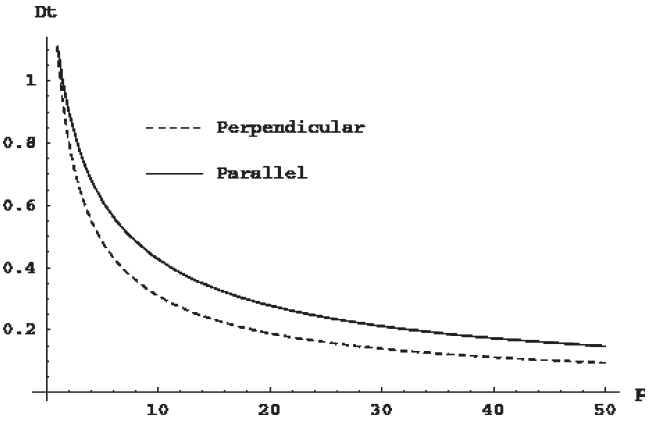

Figure 3. Parallel and perpendicular components of the translational diffusion tensor $\mathbf{D}_t$ as a function of the axial ratio $p = L/d$ for a rectangular cylinder of thickness d. For convenience, a factor $kT/4\pi\eta d$ has been factored out, yielding a dimensionless value for $\mathbf{D}_t$.

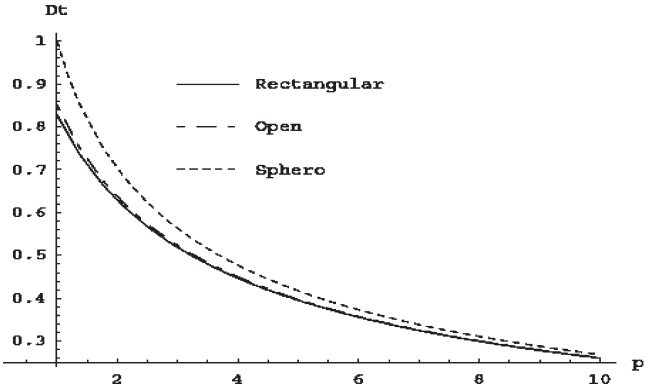

Figure 4. Average value of the $\mathbf{D}_t$ tensor for the three different shapes, where $kT/3\pi\eta d$ has been factored out, as a function of the axial ratio $p = L/d$. The open and rectangular cylinders are almost the same. The end effects become negligible at large axial ratio.

IV.2. Rotational Diffusion. The tensor components of the rotational diffusion are given as follows:

$$D_r^\perp = \frac{3kT}{\pi\eta L^3}[\ln(p) + X_r^\perp(p)] \tag{21}$$

$$D_r^\parallel = \frac{kT}{\pi\eta L^3}[1 + X_r^\parallel(p)]p^2 = \frac{kT}{\pi\eta p d^3}[1 + X_r^\parallel(\mathrm{p})] \tag{22}$$

The axial ratio dependence of the eigenvalues of the rotational diffusion tensor is shown in Figures 5 and 6. The functional forms of the shape function for each of the three shapes are given in Table 3. The precision to which the expressions reproduce the raw data is given in the column labeled "prec.", a number that is comparable to the precision of the raw data itself.

The expression for the parallel shape function for the sphero-cylinder needs immediate comment. This shape degenerates exactly to a sphere for axial ratio $p = 1$. Thus, the behavior of the shape function (see Figure 7) is rather extreme for this case and the sphere limit requires that $X_r^\parallel(1) = 0$. This requirement forces the representation to

Table 2. Translational Diffusion Shape Functions

shape	expression	prec. (%)
rectangular	$X_\tau^{\perp}(p) = 0.86609 - \frac{0.650602}{\sqrt{p}} + \frac{1.2839}{p} - \frac{0.397905}{p^2} - \frac{0.18332\ln(p)}{p^2}$	0.01
	$X_\tau^{\parallel}(p) = -0.234963 - \frac{3.14268}{\sqrt{p}} + \frac{4.29031}{p} + \frac{0.197913}{p^2} + \frac{1.96581\ln(p)}{p^2}$	0.02
	$X_\tau(p) = 0.374304 - \frac{1.11097}{\sqrt{p}} + \frac{1.71453}{p} - \frac{0.149474}{p^2} + \frac{0.491453\ln(p)}{p} - \frac{0.091666\ln(p)}{p^2}$	0.01
open	$X_\tau^{\perp}(p) = 0.864087 - \frac{0.614785}{\sqrt{p}} + \frac{1.2819}{p} - \frac{0.410315}{p^2} - \frac{0.193818\ln(p)}{p^2}$	0.01
	$X_\tau^{\parallel}(p) = -0.215396 - \frac{3.41249}{\sqrt{p}} + \frac{4.51056}{p} + \frac{0.278998}{p^2} + \frac{2.18549\ln(p)}{p}$	0.04
	$X_\tau(p) = 0.378195 - \frac{1.16052}{\sqrt{p}} + \frac{1.76859}{p} - \frac{0.135408}{p^2} + \frac{0.546373\ln(p)}{p} - \frac{0.096909\ln(p)}{p^2}$	0.02
sphero	$X_\tau^{\perp}(p) = 0.902952 - \frac{0.311044}{\sqrt[4]{p}} + \frac{0.18085}{\sqrt{p}} + \frac{0.904672}{p} - \frac{0.344085}{p^2} - \frac{0.190732\ln(p)}{p^2}$	0.01
	$X_\tau^{\parallel}(p) = -0.113192 - \frac{1.30429}{\sqrt[4]{p}} + \frac{1.19032}{\sqrt{p}} + \frac{3.12756}{p} - \frac{1.56699}{p^2} - \frac{0.930791\ln(p)}{p^2}$	0.04
	$X_\tau(p) = 0.423178 - \frac{0.481595}{\sqrt[4]{p}} + \frac{0.388005}{\sqrt{p}} + \frac{1.23423}{p} - \frac{0.56379}{p^2} - \frac{0.328064\ln(p)}{p^2}$	0.02

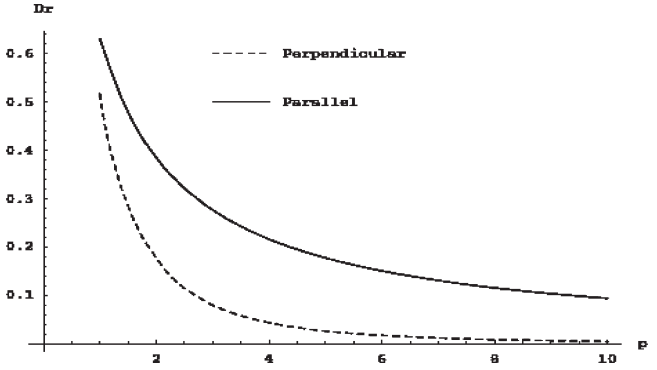

Figure 5. Perpendicular and parallel components of the rotational diffusion tensor $\mathbf{D}_r$ as a function of the axial ratio $p = L/d$ for a rectangular cylinder. The quantity $kt/\pi\eta d^3$ has been factored out for convenience of presentation.

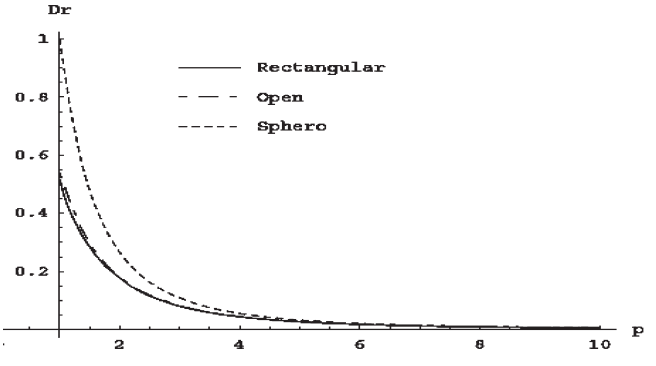

Figure 6. Perpendicular components of the $\mathbf{D}_r$ tensor for all three shapes are shown as a function of the axial ratio $p = L/d$. The quantity $kt/\pi\eta d^3$ has been factored out for convenience of presentation. The open and rectangular cylinder are almost the same. Even at low values of the axial ratio, the end effects become negligible.

be constructed with the Ln(p) function if one desires to preserve the asymptotic form expressed in eq 22. The perpendicular shape function does not have this requirement, but rather $X_r^{\perp}(1) = {}^1/_3$, which is satisfied by the equation in Table 3 to five decimals. Thus that shape function can be represented with the same type of expressions for used for the rectangular or open cylinder.

IV.3. Intrinsic Viscosity. The intrinsic viscosity is given by a simple formula in terms of the dimensionless viscosity factor $\chi(p)$ computed in eq 15, Avogadro's number N_o, the molecular weight M, and the volume of the particle, V.

$$[\eta] = \frac{N_o V \chi(p)}{M} \tag{23}$$

BEST actually computes the product $V\chi$ and the viscosity factor χ is extracted by dividing by the volume. The viscosity factor is sometimes termed the Einstein viscosity factor in recognition of his evaluation of this quantity for a sphere: $\chi = {}^5/_2$. It is important to note that the viscosity factor depends only on shape, not size, and because the molecular weight is also proportional to the volume, the intrinsic viscosity itself is a functional of shape as well. At this point, it is worth remarking that the traditional formula often used for intrinsic viscosity of rodlike macromolecules[33]

$$[\eta] = \frac{2\pi N_o L^3}{45M(\ln(p) + X_\eta)} \tag{24}$$

is derived from slender body theory and is a very poor representation of the intrinsic viscosity for small and moderate values of the axial ratio (yes, $p = 100$ is moderate!). If one tries to fit the accurate viscosity factor data to the

Table 3. Rotational Diffusion Shape Functions

shape	expression	prec. (%)
rectangular	$X_r^{\perp}(p) = -0.480483 - \frac{1.40056}{\sqrt{p}} + \frac{3.91903}{p} - \frac{2.4528}{p^3} - \frac{2.58127\ln(p)}{p^2}$	0.01
	$X_r^{\parallel}(p) = \frac{0.0332592}{\sqrt{p}} - \frac{0.906442}{p} - \frac{0.656023}{p^2} + \frac{1.69313}{p^3} - \frac{0.533147}{p^4} + \frac{1.04613\ln(p)}{p^2}$	0.04
open	$X_r^{\perp}(p) = -0.492903 - \frac{1.17543}{\sqrt{p}} + \frac{3.16941}{p} - \frac{3.29204}{p^2} + \frac{3.6909}{p^3} - \frac{1.72023}{p^4}$	0.03
	$X_r^{\parallel}(p) = \frac{0.255935}{\sqrt{p}} - \frac{0.790253}{p} - \frac{0.228575}{p^2} + \frac{0.894171}{p^3} - \frac{0.25051}{p^4}$	0.03
sphero	$X_r^{\perp}(p) = -0.372093 - \frac{0.95622}{\sqrt[4]{p}} + \frac{1.24792}{\sqrt{p}} + \frac{1.23085}{p} - \frac{1.99498}{p^2} + \frac{1.84201}{p^3} - \frac{0.664147}{p^4}$	0.02
	$X_r^{\parallel}(p) = -0.00158688\ln(p) + \frac{0.0369518\ln(p)}{\sqrt{p}} - \frac{0.239276\ln(p)}{p} + \frac{0.610134\ln(p)}{p^2} - \frac{0.808254\ln(p)^3}{p^3}$	0.03

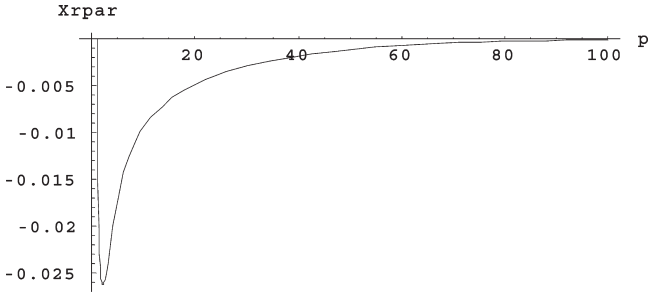

Figure 7. Shape function for the parallel component of the rotational diffusion tensor for the sphero-cylinder as a function of axial ratio p. The shape functions for the other types of cylinders are monotonic and present no special difficulty.

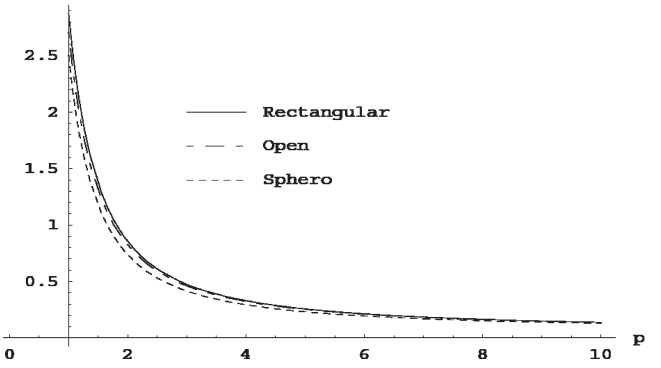

Figure 8. Viscosity factor $\chi(p)/p^2$ for the various cylinder shapes as a function of axial ratio $p = L/d$. The shape dependence is small and disappears for large axial ratio.

traditional form, one observes a very poor fit, with randomly fluctuating values of $X_\eta \approx -1$ as a function of p. The traditional formula should simply be discarded and eq 23 should be used instead for accurate values of the intrinsic viscosity of cylinders or any other rodlike objects. The asymptotic form of the viscosity factor for a cylinder is given by[29]

$$\frac{8p^2}{45\ln(p)}$$

and it is possible to construct an approximant using the kernel of this form. The form we have selected is shown in eq 25 below.

$$\chi(p) = \frac{8p^2}{45}\left(\ln(p) + \frac{8}{45\chi(1)}\right)^{-1}[1 + X_\eta(p)] \qquad (25)$$

For comparison, the explicit formula for a rectangular cylinder becomes

$$[\eta] = \frac{\pi N_o L^3 \chi(p)}{4p^2 M} = \frac{2\pi N_o L^3}{45M\left(\ln(p) + \frac{8}{45\chi(1)}\right)}[1 + \chi_\eta(p)] \qquad (26)$$

Our proposed eq 26 has the correct asymptotic form, but note that the shape function $\chi_\eta(p)$ is added in the numerator, unlike the traditional form in eq 24. Furthermore, the reciprocal part of eq 25 has been constructed to yield the exact value at $p = 1$, since $\chi_\eta(1) = 0$. This choice makes our equation valid for the entire interval $1 \le p < \infty$. The axial ratio of the dependence of the viscosity factor χ is shown in Figure 8. The viscosity factor at $p = 1$, the volume, and the shape functions for the different cylinders are shown in Table 4.

The functions in Table 4 represent the raw data extremely well. The accuracy of these calculations is estimated to be about 0.1% overall. The approximants have been constructed so that at $p = 1$, the formula yields the precise value of $\chi(1)$.

One obvious question is what "volume" should be used to extract the viscosity factor from the product $V\chi$ computed in BEST for the case of the open cylinder. Technically, the volume is zero for a two-dimensional sheet. Since the hydrodynamic interaction makes the open cylinder behave very closely to the rectangular cylinder, it is as if the effective volume of the particle in the fluid is the same as that of the rectangular cylinder. Thus, we have obtained the viscosity factor for the open cylinder using the volume of its equivalent rectangular cylinder. Note however, that the intrinsic viscosity can be computed directly from the product $V\chi$ produced by BEST, thus there is no ambiguity in the computation of the intrinsic viscosity. The precise value of this product is, by definition, the volume of the equivalent rectangular cylinder times the value of χ given by eq 25 and the expression in Table 4.

IV.4. The Choice of Mathematical Representation. In order for the interpolation formulas to represent the data to high precision, it is important to select a set of basis functions that has large values of the T statistic in the least-squares fits. We illustrate this process by discussing the fit for the $D_r^{\perp}$ raw data set for the rectangular cylinder. We note that dimensional analysis demands that the rotational diffusion coefficient be proportional to L^{-3}, thus, the raw data set is first multiplied by p^3. This yields a monotonically increasing function that looks very much like $\ln(p)$. The least-squares fit of $p^3 D_r^{\perp}$ to a basis set $= \{1, \ln(p), 1/p^{1/2}, 1/p, 1/p^2, \ln(p)/p^2\}$ yields an excellent fit with a coefficient of 3.035 for $\ln(p)$ and a T statistic of 408.6. Thus, $\ln(p)$ is an excellent basis function for the representation of the data. The next step is to set the coefficient of $\ln(p)$ exactly to 3, and subtract that from the data. Now the least-squares fit of $p^3 D_r^{\perp} - 3\ln(p)$ to the basis set $\{1, 1/p^{1/2}, 1/p, \ln(p)/p^2, 1/p^3, 1/p^4\}$ yields the results in Mathematica shown in Table 5.

We see that the T_{stat} values are much bigger than 1 in magnitude, indicating that each of the chosen basis functions has explanatory power in representing the function. Addition of other basis functions fails to improve the fit, and the T_{stat} values are small for several of the entries in that case. Thus, given the quality of the data set, the chosen set of basis

Table 4. Intrinsic Viscosity Shape Function

shape	expression	prec. (%)
rectangular $\chi(1) = 2.87613$ $V = \frac{\pi L^3}{4p^2}$	$X_n(p) = \frac{0.763598}{\sqrt[4]{p}} - \frac{0.215376}{\sqrt{p}} + \frac{4.11468}{p} + \frac{1.75913}{p^2} - \frac{6.15425}{p^3} - \frac{0.267793}{p^4} + \frac{2.42918\ \ln(p)}{p^4}$	0.02
open $\chi(1) = 2.70573$	$X_n(p) = \frac{1.33283}{\sqrt[4]{p}} + \frac{3.49041}{p} + \frac{4.23438}{p^2} - \frac{10.3252}{p^3} + \frac{1.26762}{p^4} - \frac{0.416735\ \ln(p)}{p^2}$	0.07
sphero $\chi(1) = {}^1/_2$ $V = \frac{\pi L^2}{4p^2}\left(1 - \frac{1}{3p}\right)$	$X_n(p) = \frac{0.784721}{\sqrt[4]{p}} - \frac{0.261673}{\sqrt{p}} + \frac{3.067}{p} + \frac{1.11557}{p^2} - \frac{3.8654}{p^3} - \frac{0.840208}{p^4} + \frac{2.36995\ \ln(p)}{p^2}$	0.03

Table 5. Analysis of $D_r^{\perp}$ Raw Data[a]

parameter	value	standard error	T_{stat}
1	−1.44145	0.00124	1160.68
$1/p^{1/2}$	−4.20168	0.0159	−263.593
$1/p$	11.7571	0.0571	205.739
$1/p^3$	−7.35841	0.0378	−194.35
$1/p^4$	1.7611	0.0131	134.03
$\ln(p)/p^2$	−7.7438	0.0802	−96.53

[a] $R^2 = 1.0$ and estimated variance $= 9.77 \times 10^{-8}$.

functions is maximal and appropriate. The coefficients of this fit are divided by 3 to match the chosen functional form for $D_r^{\perp}$ in eq 20 and are presented in the table for the expression of $X_r^{\perp}(p)$. In addition, note that the quantity $p^3 D_r^{\perp} - 3\ln(p)$ is a smoothly varying function of magnitude ≈ -1, and thus the low variance of the above fit guarantees that the resulting function will represent the data to very high precision. This procedure appears to be more precise than the Padé approximants used by other workers.

The principles outlined in the above example were followed to construct the interpolation functions for the other diffusion coefficient tensor components. In each case, the T_{stat} variable singled out the proper form of the $\ln(p)$ function that should be present, and the final fits were done to quantities of order 1, allowing high precision in the final results. In the case of $D_r^{\parallel}$, the proper form does not contain $\ln(p)$, but the first term should be the constant 1, instead. Thus our data sets contain the information to choose the proper forms of the formulas presented above, yielding a very robust representation.

V. Comparison with the Literature

As mentioned in the Introduction, there are several computations of the transport properties of cylinders that have appeared in the literature. In this section, we compare our results with several different computational approaches for each of the different shapes. In the case of the open cylinder, we are not aware of other formulas in the literature, however, our results demonstrate that the differences with the rectangular cylinder are very small. The similarity between these two shapes was previously noticed and commented on by TG.[30] Our comparison shows that previous work generally has significant inaccuracies and/or limited axial ratio range.

For the rectangular cylinder the main pre-existing computations are those of Tirado and Garcia de la Torre[30,31] (TG), Ortega and Garcia de la Torre[33] (OG), Broersma[26−28] (B), Yoshiszaki and Yamakawa[32] (YY), and Mansfield and Douglas[35] (MD). The calculations of TG and OG based on the bead methodology have a limited axial ratio range, with the newer ones extending to axial ratio 1, and up to 20, and cover the average translational diffusion tensor, the two components of the rotational diffusion tensor and the intrinsic viscosity. The calculations of Yamakawa and co-workers are theoretical based on the preaveraged HI with the Oseen Burgers method and include the sphero-cylinder and rectangular cylinder. The more accurate newer work of MD

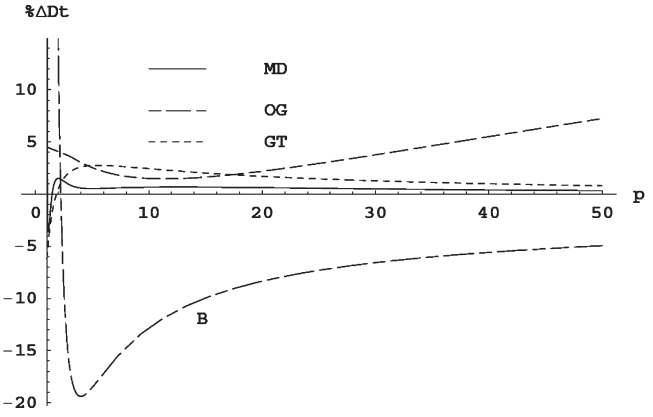

Figure 9. Percent difference for the average translational diffusion tensor of literature values to our accurate formulas as a function of axial ratio for the rectangular cylinder. The symbols represent the referenced works of Mansfield and Douglas (MD), Ortega and Garcia de la Torre (OG), Tirado and Garcia de la Torre (TG), and Broersma (B).

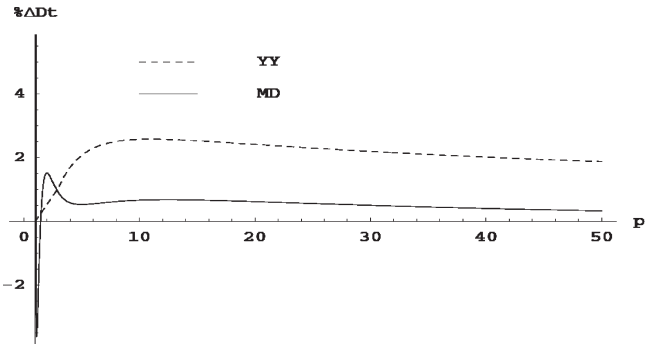

Figure 10. Percent difference for the average translational diffusion tensor of literature values to our accurate formulas as a function of axial ratio for the spherocylinder is shown. The symbols represent the referenced works of Yoshisaki and Yamakawa (YY) and Mansfield and Douglas (MD).

extends through a large axial ratio range and is based on a stochastic method that exploits an analogy with the electrostatic properties of a metallic body—their methodology computes only the average of the tensor, not the individual components. Their computations include the rectangular cylinder and spherocylinder. The older and less accurate formulas of Broersma (B) are also included in the comparison. In the figures that follow we compare our results with the existing formulas just mentioned.

Translational Diffusion. The translational diffusion coefficient is the easiest transport property to compute accurately in that the tensor portion of the hydrodynamic interaction makes an almost negligible effect.[10] This is born out in Figures 9 and 10. The best result available in the literature is the Mansfield and Douglas[35] (MD) formula valid for $p > 1.65$. Their largest inaccuracies occur for small axial ratios, but for large axial ratios the inaccuracy is less than 1%. Their

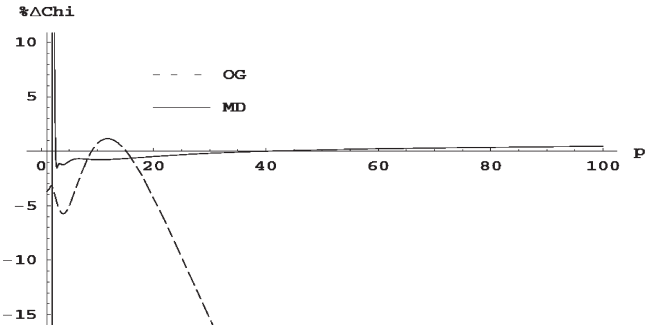

Figure 11. Percent difference for the viscosity factor between our results and the literature for the rectangular cylinder as a function of axial ratio. The symbols represent the referenced works of Yoshisaki Ortega and Garcia de la Torre (OG) and Mansfield and Douglas (MD).

path integral method discards the tensor portion of the Oseen tensor and thus the difference between our formulas and theirs is actually an inaccuracy in the MD results. We feel that our formulas are more accurate than the calculations by MD because our BE methodology has been shown[6] to produce typical errors of only 0.01% when compared to analytical results for ellipsoids. However the inaccuracy in the MD formulas is small when compared to experimentally achievable uncertainties of around 2%. Our formulas have a significant advantage over the MD formulas only in the small axial ratio region. The small inaccuracy at low axial ratio in the MD formulas is likely the choice of Pade approximant to represent their raw data—the path integral method itself should be accurate to better than 1% for all axial ratios. Figure 9 also shows that the older theoretical work of Broersma[28] (B) is fairly inaccurate for all axial ratios and very slowly converges to the correct asymptotic limit at large axial ratio. Figure 9 shows that the original TG formula for rectangular cylinders has reasonable accuracy over the entire range of axial ratio and has the correct asymptotic limit. The newer work of Ortega and Garcia de la Torre[33] has larger inaccuracies and does not have the correct asymptotic limit. The authors intend their formula to be valid in the range of $1 < p < 20$, but the graph shows increasing error for extrapolation beyond $p = 20$, unlike the TG formula. For the spherocylinder, Figure 10, the older calculations of Yamakawa and Yoshisaki[32] (YY) are only moderately inaccurate and have the correct asymptotic limit, while the recent formulas of Manfield and Douglas[35] (MD) are very accurate except in the small axial ratio region. Again, the inaccuracy there is probably not intrinsic to their method, but rather associated with the form of the Pade approximant they chose.

Viscosity Factor. Figures 11 and 12 show that the formulas of Mansfield and Douglas[35] (MD) are the best of previously available computations. The MD formulas for both shapes are excellent except for small axial ratios, where the inaccuracy is quite large. MD state that their formulas are valid for $p > 2.72$. It is worth noting that the MD pade approximants are probably the limiting factors in this comparison, since MD recognize in their paper that the much higher precision of their raw data could not be captured for all axial ratios in generating their formulas—the implementation of the path integral method can yield higher precision than their formulas express. For the rectangular cylinder, Figure 11 shows that the formula of OG does not have the correct asymptotic form and has inaccuracies that exceed 5% in its region of validity ($1 < p < 20$). Even though the OG work was computed for axial ratios up to 20, it is instructive to see the behavior outside of this range to ward against insecure

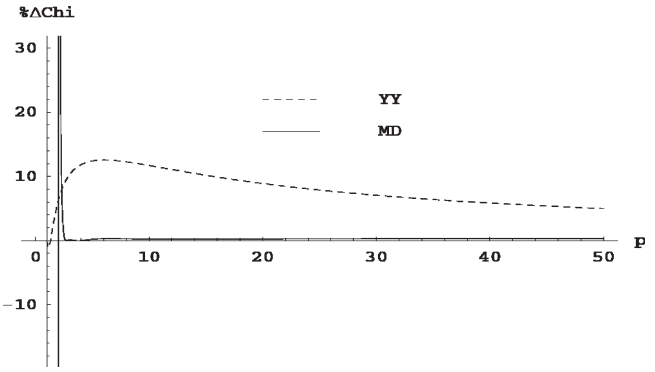

Figure 12. Percent difference for the viscosity factor between our results and the literature for the spherocylinder as a function of axial ratio. The symbols represent the referenced works of Yoshisaki and Yamakawa (YY) and Mansfield and Douglas (MD).

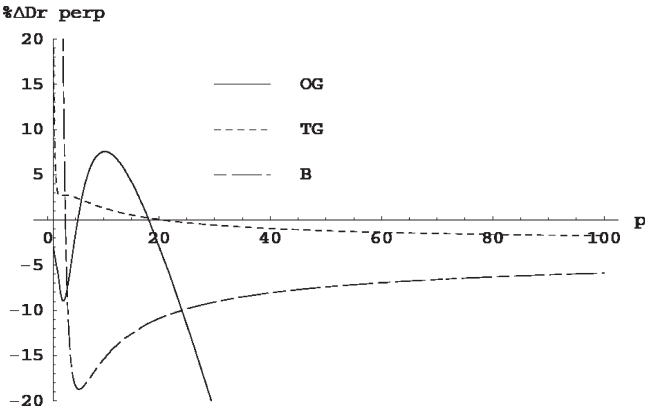

Figure 13. Percent difference for the perpendicular component of the rotational diffusion tensor between our results and the literature for the rectangular cylinder as a function of axial ratio. The symbols represent the referenced works of Ortega and Garcia de la Torre (OG), Tirado and Garcia de la Torre (TG), and Broersma (B).

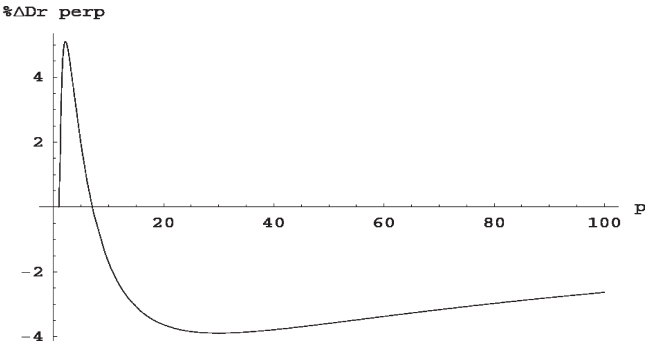

Figure 14. Percent difference for the perpendicular component of the rotational diffusion tensor between our results and the work of Yoshisaki and Yamakawa (YY) for the spherocylinder as a function of axial ratio.

extrapolations. The formula of YY[32] for the spherocylinder is quite interesting because it corresponds to an early implementation of the boundary element method used in this work. The authors, given the small size of computer memory at that time, were forced to assume that the surface stress forces where axially symmetric, with the consequence that their values have significant inaccuracies for small axial ratios but their results appear to converge to the correct asymptotic limit.

Rotational Diffusion. Figures 13 and 14 show that the original Tirado and Garcia de la Torre[31] (TG) formula for the rectangular cylinder and the Yoshisaki and Yamakawa[32] (YY) formula for the spherocylinder have moderately accurate over most of the axial ratio range. It appears that the YY formula tends to the correct asymptotic value, but the TG formula slowly deviates from it at a large axial ratio. The TG formula also has large inaccuracies near $p = 1$. The formula of Ortega and Garcia de la Torre[33] (OG) does better at $p = 1$, but for the rest of the axial ratio region, the OG formula has larger discrepancies than the original TG computations and does not have the correct asymptotic value. The rectangular cylinder computation via the Oseen−Burgers approximation of Yamakawa[29] has good asymptotic behavior and is meant to be correct for $p > 62$ − it indeed does badly at lower axial ratios.

Yamaka and Yoshisaki[32] did not produce a formula for the parallel component of D_r for the sphero-cylinder, but they did present a few tabulated values for low axial ratio. The inaccuracy in these results is moderate with a maximum of 3.3% at $p = 3.2$. The reasonable accuracy obtained in their computations for the spherocylinder are a testament to the care they took in performing their work with the very limited computer resources of 30 years ago.

VI. Conclusions

We have presented an extremely precise and accurate numerical solution to the exact integral equations for Stokes flow with stick boundary conditions to compute the translational and rotational diffusion tensors, and the intrinsic viscosity for three types of cylinders with axial ratios between 1 and 100. By a careful design of the triangular tessellations and extrapolation to infinite number of triangles we are able to obtain values with estimated uncertainties of 0.07% or better which far surpasses the precision previously available in the literature. The data are summarized by fairly simple mathematical expressions as a function of the axial ratio of the cylinders which are constructed to satisfy the correct asymptotic expressions, yielding formulas that are valid for $1 \leq p < \infty$. The end effects are large at small axial ratios but quickly become unimportant as the axial ratio increases beyond 10 for all properties. The spherocylinder is readily distinguished from the rectangular cylinder at small axial ratio, but the open cylinder is differs very little from the rectangular cylinder. Evidently hydrodynamic screening is completely dominant and the cavity makes little difference. The comparison of our results with previous formulas available in the literature for different types of cylinders shows that except for the path integral method results, other work has significant inaccuracies. Our formulas are generally more accurate at small axial ratios than the formulas that summarize the path integral method results, and the boundary element method can produce full tensor properties, in particular for the rotational diffusion, while the path integral method cannot.

The aim of this work was to introduce formulas that are more accurate than the typical experimental precision in the measurements of transport properties—this allows for the detection of subtle effects as instrumental methods improve. When theoretical expressions have inaccuracies that are larger or comparable to experimental errors, interesting features of real systems can easily be missed. The expressions obtained in this work will be useful in the description of the transport properties of interesting macromolecules such as carbon nanotubes, microtubules, and viruses. For large axial ratios, however, it is very likely that flexibility should be taken into account for the proper description of the transport properties—the work presented here can serve as a useful reference state to introduce flexibility by perturbation methods, for example. In the case of carbon nanotubes, solutions in organic solvents are more common than in aqueous environments. For the organic solvent case, one suspects that the slip boundary condition would be more appropriate—such results will be presented in a separate publication. The boundary element method is unique in being able to handle general hydrodynamic boundary conditions.

Acknowledgment. This work was partially funded by NIH MBRS SCORE Grant S06 GM52588 to S.R.A.

References and Notes

(1) Harris, P. J. F. *Carbon Nanotubes and Related Structures*; Cambridge University Press, Cambridge, U.K., 1999.
(2) Hirth, L.; Richards, K. E. *Adv. Virus Res.* **1981**, *26*, 145–199.
(3) Strauss, S. K.; Scott, W. R. P.; Symons, M. F.; Mann, D. A. *Eur. Biophys. J.* **2008**, *27*, 521–527.
(4) Eimer, W.; Pecora, R. *J. Chem. Phys.* **1991**, *94*, 2324–2329.
(5) Amos, L. A. *Org. Biomol. Chem.* **2004**, *2*, 2153–2160.
(6) Aragón, S. R. *J. Comput. Chem.* **2004**, *25*, 1191–1205.
(7) Aragon, S. R.; Hahn, D. K. *Biophys. J.* **2006**, *91*, 1591–1603.
(8) Hahn, D. K.; Aragon, S. R. *J. Chem. Theor. Comput.* **2006**, *2*, 1416–1428.
(9) Aragon, S. R.; Hahn, D. K. *J. Phys. Chem. B* **2009**, *113*, 2657–2663.
(10) Aragon, S. R.; Hahn, D. K. *J. Chem. Theor. Comput.* **2006**, *2*, 12–17.
(11) Kim, S.; Karilla, S. J. *Microhydrodynamics*; Butterworth-Heinemann: New York, 1991.
(12) Youngren, G. K.; Acrivos, A. *J. Fluid Mech.* **1975**, *69*, 377–402.
(13) Wegener, W. A. *Biopolymers* **1986**, *25*, 627–637.
(14) Rotne, J.; Prager, S. *J. Chem. Phys.* **1969**, *50*, 4831–4837.
(15) Brune, D.; Kim, S. *Proc. Natl. Acad. Sci. U.S.A.* **1993**, *90*, 3835–3839.
(16) Allison, S. A. *Macromolecules* **1999**, *32*, 5304–5312.
(17) Hu, C. M.; Zwanzig, R. *J. Chem. Phys.* **1974**, *60*, 4354–4357.
(18) Allison, S. A.; Nambi, P. *Macromolecules* **1992**, *25*, 3971–3978.
(19) Allison, S. A.; Nambi, P. *Macromolecules* **1994**, *27*, 1413–1422.
(20) Allison, S. A.; Tran, V. T. *Biophys. J.* **1995**, *68*, 2261–2270.
(21) Allison, S. A.; Mazur, S. *Biopolymers* **1998**, *46*, 359–373.
(22) Perrin, F. *J. Phys. Radium* **1936**, *7*, 1–11.
(23) Simha, R. *J. Phys. Chem.* **1940**, *44*, 25–34.
(24) Saito, N. *J. Phys. Soc. Jpn.* **1951**, *5*, 297–301.
(25) Batchelor, G. K. *An introduction to fluid mechanics*; Cambridge University Press: New York, 1999.
(26) Broersma, S. J. *J. Chem. Phys.* **1960**, *32*, 1626–31.
(27) Broersma, S. J. *J. Chem. Phys.* **1960**, *32*, 1632–5.
(28) Broersma, S. J. *J. Chem. Phys.* **1981**, *74*, 6989–6990.
(29) Yamakawa, H. *Macromolecules* **1975**, *8*, 339–342.
(30) Tirado, M. M.; Garcia de la Torre, J. *J. Chem. Phys.* **1979**, *71*, 2581–2587.
(31) Tirado, M. M.; Garcia de la Torre, J. *J. Chem. Phys.* **1980**, *73*, 1986–1993.
(32) Yoshizaki, T.; Yamakawa, H. *J. Chem. Phys.* **1980**, *72*, 57–69.
(33) Ortega, A.; Garcia de la Torre, J. *J. Chem. Phys.* **2003**, *119*, 9914–9919.
(34) Kang, E.-H.; Mansfield, M. L.; Douglas, J. F. *Phys. Rev. E* **2004**, *69*, 031918.
(35) Mansfield, M. L.; Douglas, J. F. *Macromolecules* **2008**, *41*, 5422–32.
(36) Mansfield, M. L.; Douglas, J. F. *Phys Rev. E* **2008**, *78*, 046712.
(37) Oseen, C. W. *Hydrodynamik*; Academiches Verlag: Leipzig, Germany, 1927.
(38) Brenner, H. *J. Colloid Interface Sci.* **1967**, *23*, 407–436.
(39) Allison, S. A. *Macromolecules* **1998**, *31*, 4464–4474.
(40) Wolfram Research, http://wolfram.com